RSC Advances

PAPER

View Article Online
View Journal | View Issue



Cite this: *RSC Adv.*, 2023, **13**, 2803

# *In vitro* magnetic hyperthermia properties of angle-shaped superparamagnetic iron oxide nanoparticles synthesized by a bromide-assisted polyol method†

Hoonsub Kim,‡[a] Pyung Won Im,‡[b] Chaedong Lee,[a] Hwichan Hong,[a] Wooseung Lee,[a] Changhyuk Koo,[a] Sang Yoon Park,[e] Hyung-Jun Im,*[abc] Sun Ha Paek*[bcd] and Yuanzhe Piao *[ae]

Currently, research on superparamagnetic iron oxide nanoparticles (SPIONs) for magnetic hyperthermia applications is steadily increasing. In this work, SPIONs were synthesized by the bromide-assisted polyol method and angle-shaped SPIONs were successfully generated with the optimized concentration of bromide. The influence of bromide concentration on the shape of the generated SPIONs as well as the heating characteristics under an alternating magnetic field (AMF) was thoroughly investigated. At a concentration of 20 mg $mL^{-1}$ of the angle-shaped SPIONs, the highest temperature curve up to 23 °C was observed under AMF with 140 Oe and 100 kHz for 10 min. With the biotoxicity assay, no significant cytotoxicity was observed in the normal fibroblast of HFB-141103 as well as tumor cells of U87MG and FSall treated with the angle-shaped SPIONs at a concentration below 100 μg $mL^{-1}$. However, significantly decreased cellular viability was observed in tumor cells of U87MG and FSall treated with 100 μg $mL^{-1}$ of the angle-shaped SPIONs under AMF with 140 Oe and 100 kHz. Based on these results, it is thought that the angle-shaped SPIONs synthesized by the bromide-assisted polyol method will provide highly efficient magnetic hyperthermia therapy for cancers under biologically safe AMF with 140 Oe and 100 kHz.

Received 12th November 2022
Accepted 30th December 2022

DOI: 10.1039/d2ra07190h

rsc.li/rsc-advances



## 1 Introduction

Iron oxide nanoparticles (IONPs) have been intensively studied for various biomedical applications, such as magnetic resonance imaging,[1] magnetically-guided drug delivery,[2] bio-separation,[3] biosensor,[4] tissue repair,[5] and magnetic hyperthermia therapy.[6,7] Magnetic hyperthermia (MH) is a treatment of cancer by generating thermal energy under the alternating magnetic field (AMF) of magnetic particles. MH is induced because the magnetic moment of these nanoparticles tends to align with the direction of the magnetic field, resulting in Néel relaxation where the magnetic moment changes or Brownian relaxation where the entire particle rotates.[8] Also, MH leads to the damage and apoptosis of tumor cells.[9,10]

MH has several advantages over conventional treatments such as surgery, chemotherapy, and radiation therapy. The advantage of MH is providing opportunity for tumor targeting through blood circulation or direct local injection without surgery with no side effects of drugs or radiation.[11,12] In MH, the heat transfer of magnetic nanoparticles (MNPs) is characterized by the specific absorption rate (SAR). A condition of MNPs for practical application is that they exhibit high SAR values at relatively low concentrations of nanoparticles and low magnitude AMF during measurements.[13,14] If these demands are met, MH therapy, which can minimize the side effects of conventional treatments and provide high efficiency for tumor cell damage, will be facilitated. Heavy metals such as cobalt or manganese have high SAR values because they are magnetic materials with high saturation magnetization, but the introduction of heavy metals causes toxicity to the human body.[15,16] Therefore, various studies have continuously been conducted to investigate magnetic properties by controlling the size and

[a]*Department of Applied Bioengineering, Graduate School of Convergence Science and Technology, Seoul National University, Suwon-si, Gyeonggi-do, 16229, Republic of Korea. E-mail: iiihjjj@snu.ac.kr*

[b]*Cancer Research Institute, Seoul National University, Seoul, 03080, Republic of Korea. E-mail: paeksh@snu.ac.kr*

[c]*Department of Molecular Medicine and Biopharmaceutical Sciences, Graduate School of Convergence Science and Technology, Seoul National University, Seoul 08826, Republic of Korea*

[d]*Department of Neurosurgery, Hypoxia/Ischemia Disease Institute, Seoul National University, Seoul 03080, Republic of Korea*

[e]*Advanced Institutes of Convergence Technology, Suwon-si, Gyeonggi-do, 16229, South Korea. E-mail: parkat9@snu.ac.kr; Tel: +82 31 888 9141*

† Electronic supplementary information (ESI) available. See DOI: https://doi.org/10.1039/d2ra07190h

‡ These authors contributed equally to this work.

shape of IONPs, which are safer than magnetic nanoparticles using heavy metals.[17] For this reason, studies have been conducted to improve the size and shape-dependent magnetic properties of IONPs, for example, Wang *et al.* synthesized cubic IONPs for large saturation magnetization,[18] and Toulemon *et al.* induced enhanced collective magnetic properties by assembling iron oxide nanoparticles in chains.[19] Nemati *et al.* went so far as to analyze the magnetic properties by tuning the size and shape of the iron oxide nanoparticles,[20] Sheng *et al.* reported a systematic study of the size dependence of heat generation by magnetic iron oxide nanoparticles under AMF,[21] and Yong *et al.* fabricated uniform $Fe_3O_4$ nanodiscs.[22] Although there are already some reports about the magnetic properties of various-shaped MNPs, to use them for biomedical applications, additional tedious surface modification processes are often required to make them biocompatible.[23–29] Herein, we report a facile bromide-assisted polyol process for the preparation of angle-shaped SPIONs. During the preparation, biocompatible PEG molecules are attached to the generated IONPs. As a result, these IONPs are well dispersed in aqueous solution and can be easily used in various biomedical fields. Polyethyleneglycol (PEG) and branched-polyethyleneimine (b-PEI) used in the synthesis help make the surface of IONPs biocompatible. PEG is a solvent used for polyol synthesis, acts as a reducing agent, and plays a role in enhancing water dispersibility and biocompatibility on the surface of nanoparticles without a separate process after synthesizing IONPs.[29–32] Also, b-PEI is a polymer that has repetitive amino groups (Fig. S1, ESI†), which controls the surface charge and enables amide bonding. Also, polyethyleneimine (PEI) has been used as an adhesion promoter because it has a weak bond with negatively charged cells on the outer surface to adhere to the plate.[33,34] Moreover, PEI is widely used as a transfection agent because of its low toxicity and cationic polymer effect.[35–37]

In this article, the optimization of bromide ion concentration used in the synthesis of angle-shaped superparamagnetic iron oxide nanoparticles (SPIONs) and the characteristics of SPIONs as a heat source for MH therapy were studied. The angular shape of the iron oxide nanoparticles is a result of the binding of bromide ions with the iron ions exposed on the surface of the growing iron oxide nanoparticles.[38] The molar ratio of bromide ions and iron precursors in the synthesis of the angle-shaped SPIONs affected the morphology of SPIONs and the heat generation characteristics when AMF was applied. For the cytotoxicity test of angle-shaped SPIONs, the biocompatibility studies were performed using three types of cell lines.

# 2 Experimental

## 2.1. Materials

All chemical reagents were used without further purification. Iron(III) acetylacetonate (>99%) was purchased from STERM-CHEM. Polyethyleneglycol 600 (PEG), potassium bromide (KBr), ethanol (EtOH, 99.9%), and ether were purchased from Samchun Chemical. b-PEI was purchased from Sigma Aldrich. DMEM high glucose, RPMI 1640, and phosphate-buffered saline (PBS) were purchased from HyClone. Fetal bovine serum (FBS), antibiotic-antimycotic (AA), and trypan blue stain were purchased from Gibco.

## 2.2. Synthesis of the angle-shaped SPIONs with potassium bromide

In a typical synthesis, 1 mmol iron(III) acetylacetonate precursor was dissolved in a solution of 10 g PEG and 2 g b-PEI. Then, 0.25 to 4 mmol KBr was added to the solution to make a KBr mixture of 20.8 mM to 666.7 mM concentration. The mixture was heated to 95 °C under low pressure (−76 cm Hg) for 1 hour to remove $H_2O$ present in PEG and b-PEI. After this degassing step, the temperature was raised to 265 °C at a heating rate of 5 °C $min^{-1}$. In this process, the lucent red solution turned brown at 140 °C. Lastly, a dark brown solution was obtained. After removing the heating mantle, the reactant was cooled to room temperature. An ethanol–ether mixture was added to the reactant, and centrifugation was carried out at RCF 8000 to separate the solvent and nanoparticles.

## 2.3. Synthesis of the amine-functionalized SPIONs

This synthesis of the amine-functionalized SPIONs (A-SPIONs) was carried out by the previously reported method.[39] Briefly, 1 mmol iron(III) acetylacetonate was mixed with 10 g PEG and 2 g b-PEI. As mentioned in the synthesis of angle-shaped SPIONs above, the heating and washing processes were carried out on the mixture.

## 2.4. Magnetic heating measurements

The magnetic nanoparticles synthesized above were dispersed in DW, and the samples were prepared by adjusting the concentration to 20 mg $mL^{-1}$. Microtubes containing 1 mL of each prepared sample were placed in the center of the coil of a magnetic field generator (Anytech), and AMF was applied for 600 s. The temperature change was measured for 600 s under AMF and 400 s after turning off AMF.

## 2.5. Cellular viability test and MH test

Three cell lines, U87MG, FSall, and HFB-141103, were used for the cytotoxicity test and the MH test. U87MG and HFB-141103 were cultured in DMEM, 10% FBS, 1% AA media, and FSall was cultured using different media that is RPMI, 10% FBS, and 1% AA media. All the cells were incubated in a 5% $CO_2$ incubator at 37 °C. CCK and MTT assays are common methods to measure the cytotoxicity of the drugs, but the uptake of the remaining IONPs in this test may interfere with detection. For this reason, after stained with trypan blue, a mechanical cell counter (AAA, Biotech) was used to count cells. Cells were cultured in 100 pie dishes and sub-cultured to 6-well plates with $1 \times 10^6$ cells per well when cell confluence reached 80%. Cells were incubated for one day to attach to the plate and the media changed to various concentrations of angle-shaped SPIONs added media. After one day of incubation, the residual angle-shaped SPIONs were washed out by PBS and the cells were harvested for cell counting. The MH test on the three cell lines used the same process as the cell counting process above, with

 

the addition of media at a concentration of 100 μg $mL^{-1}$ angle-shaped SPIONs into 24-well plates for the hyperthermia test. An alternating magnetic field generator was used for the exposure magnetic field up to 20 min. The same mechanical cell counter was used to observe the cell viability each day after AMF was applied.

### 2.6. Characterization

All transmission electron microscopy (TEM) images were gained using a LIBRA 120 (Carl Zeiss) at an acceleration voltage of 120 kV. The samples for TEM studies were prepared by drying a drop of the nanoparticle suspension on a piece of the carbon-coated copper grid at ambient conditions. The X-ray diffraction (XRD) patterns were taken by an X-ray diffractometer (New D8 Advance, Bruker) with Cu-Kα radiation ($\lambda = 1.5406$ Å) at 40 kV and 40 mA. Magnetic measurement was conducted using a VSM-7410 (Lake Shore Cryotronics). Magnetic nanoparticles at 100 kHz and 140 Oe conditions using a magnetic field generator (Multi Hi Frequency Generator, 2 × 4 channels, 30–370 kHz, 90 Oe or higher, Anytech) were tested for the heating characteristics. The temperature change of the solution in which magnetic nanoparticles are dispersed during the MH test was measured at one second intervals using a custom probe (M924 Semiconductor OEM Unit, Lumasense Tech) capable of measuring the range from −45 °C to 330 °C. Statistical analysis was determined by Student's *t*-test and one-way ANOVA using GraphPad Prism. The level of significance was fixed as $P < 0.05$.

## 3 Results and discussion

### 3.1. Synthesis of the angle-shaped SPIONs

Angle-shaped SPIONs were synthesized by adding potassium bromide to the synthesis process to control the shape, and A-SPIONs were prepared for comparison with angle-shaped SPIONs. As can be seen in Fig. 1, the synthesis of SPIONs was performed by applying the previously reported method of PEG-assisted polyol[27] to iron(III)I acetylacetonate used as a precursor and PEG used as a capping and reducing agent. b-PEI allowed the presence of a large number of amine groups on the surface of the SPIONs, and KBr was responsible for making the SPIONs angular. As shown in Fig. S2 (ESI†), the absolute value of zeta potential of SPIONs synthesized using b-PEI (28.3 mV) is higher than that of SPIONs synthesized without b-PEI (−16.7 mV) due to the influence of amine groups on the surface of the nanoparticles. Accordingly, it can be seen that the water dispersion stability is further improved. It has been previously reported that halide ions stabilize the (100) facet of nanocrystals in the synthesis of IONPs to form cube-shaped nanoparticles.[40,41] To find out more about how the concentration of KBr affects the nanoparticle morphology, KBr, the halide ion source, was adjusted from 20.8 to 333.3 mM (Fig. S3, ESI†).

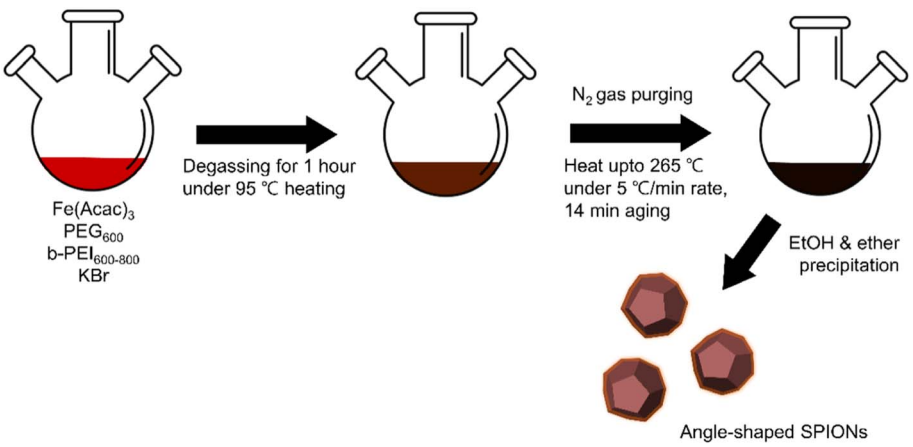


Fig. 1 Schematic illustration of the bromide-assisted synthetic procedure for angle-shaped superparamagnetic iron oxide nanoparticles.

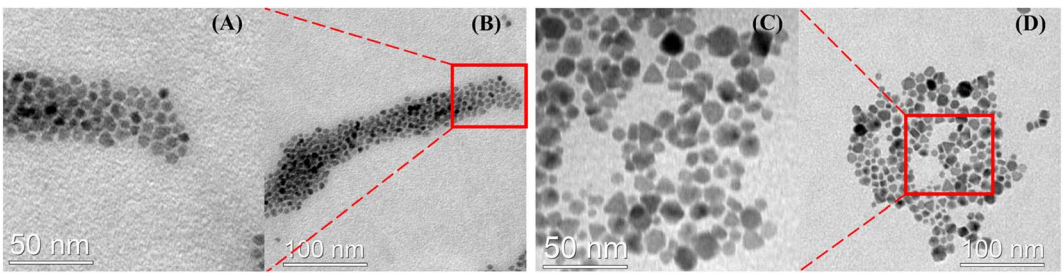


Fig. 2 Transmission electron microscopy images of (A) and (B) amine-functionalized SPIONs and (C) and (D) bromide-assisted angle-shaped SPIONs.

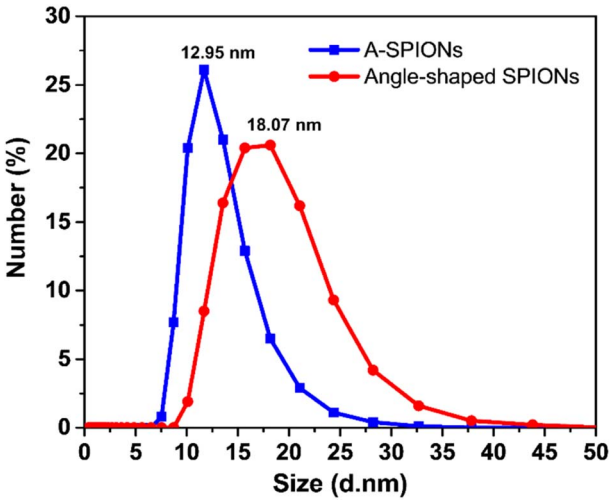


Fig. 3 Hydrodynamic size-distribution of the A-SPIONs and angle-shaped SPIONs in DI water.

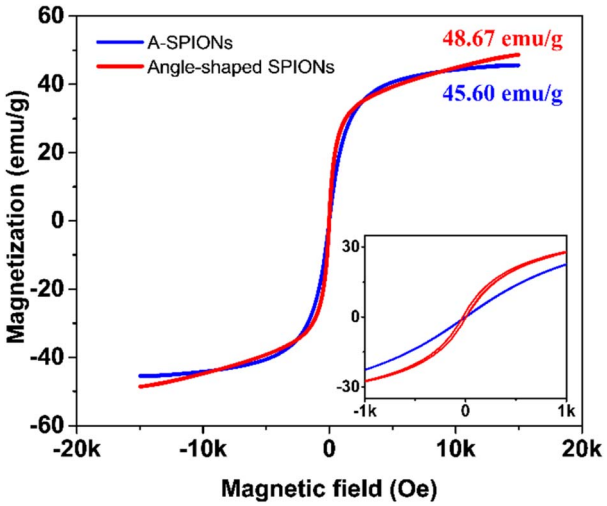


Fig. 5 Magnetic behaviors of A-SPIONs and angle-shaped SPIONs synthesized by adding 333.3 mM KBr.

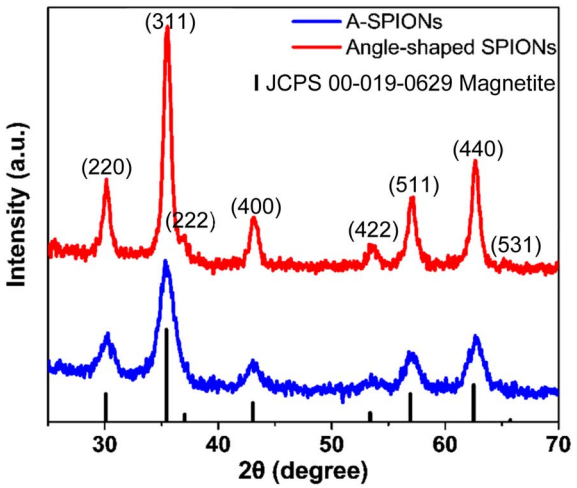


Fig. 4 XRD patterns of A-SPIONs and angle-shaped SPIONs.

TEM images show how the presence or absence of bromide affects the shape of SPIONs. SPIONs synthesized without KBr have a spherical shape (Fig. 2A and B), while those synthesized with KBr show IONPs of various angled morphology (Fig. 2C and D). It was confirmed that the SPIONs synthesized with KBr had a predominantly angular shape and the morphological difference between angle-shaped SPIONs and A-SPIONs.

The hydrodynamic size distribution of A-SPIONs and angle-shaped SPIONs was measured by DLS. The hydrodynamic size dispersed in DI water was determined to be 12.95 nm for A-SPIONs and 18.07 nm for angle-shaped SPIONs. DLS measurements show a narrow size distribution of A-SPIONs, and angle-shaped SPIONs show a relatively wide size distribution due to shape differences (Fig. 3).

### 3.2. Crystal structure study of the angle-shaped SPIONs

XRD measurements were performed to confirm the crystal structure of angle-shaped SPIONs and A-SPIONs. The XRD patterns of angle-shaped SPIONs and A-SPIONs were summarized in Fig. 4. The overall pattern of the angle-shaped SPIONs was well indexed with $Fe_3O_4$ (JCPDS # 00-019-0629). (220), (311), (220), (400), (422), (511), (440), and (531), as revealed in the XRD pattern. The (111) peak could not be assigned because it overlapped with the pattern of PEG, a surface organic molecule, and was indistinguishable.

### 3.3. Magnetization study of angle-shaped SPIONs

To analyze the magnetic properties of A-SPIONs and angle-shaped SPIONs, M–H loops were drawn by applying a field range from −15 kOe to 15 kOe at 298 K (Fig. 5). The data were presented as emu per g of iron. The saturation magnetization ($M_s$) values in the M–H loop show 45.60 emu $g^{-1}$ for A-SPIONs and 48.67 emu $g^{-1}$ for angle-shaped SPIONs. It is hypothesized that angle-shaped SPIONs could provide high magnetization among IONPs of a similar size range due to their angular morphology.[18,42] Therefore, angle-shaped SPIONs described above are materials with excellent magnetic properties for magnetic separation and recycling as nanoparticles do not have strong magnetic interactions in dispersion. The experimental results show that the water suspensions of angle-shaped SPIONs are well dispersed but agglomerate under the influence of the magnetic field by the magnets (Fig. S4, ESI†).

### 3.4. Heating study of angle-shaped SPIONs

Fig. 6A and B show the temperature change of angle-shaped SPIONs synthesized by adding from 0 to 666.7 mM KBr under a magnetic field condition of 140 Oe at a fixed frequency of 100 kHz for 15 min. Each sample was measured by dispersing it in distilled water at a concentration of 20 mg $mL^{-1}$. Fig. 6 shows curves of different shapes depending on the concentration of KBr used for the synthesis of SPIONs. As the concentration of KBr increased from 20.8 mM to 333.3 mM, the temperature change led to an increase, but 666.7 mM KBr showed a decrease

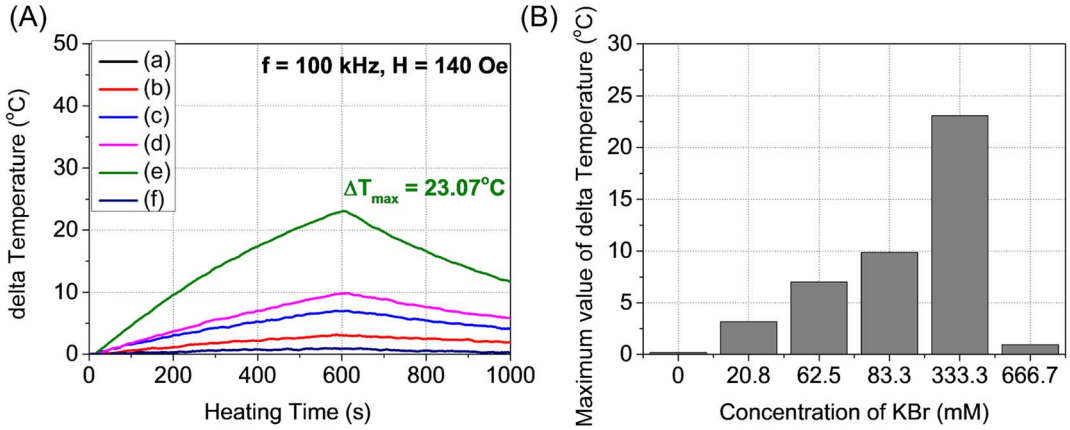


Fig. 6 Heating characteristics of angle-shaped superparamagnetic iron oxide nanoparticles synthesized by adding (a) 0 mM, (b) 20.8 mM, (c) 62.5 mM, (d) 83.3 mM, (e) 333.3 mM, and (f) 666.7 mM KBr. (A) Temperature changes for each samples under a magnetic field condition of 140 Oe at a fixed frequency of 100 kHz for 15 minutes and (B) maximum value of delta temperature for each samples.

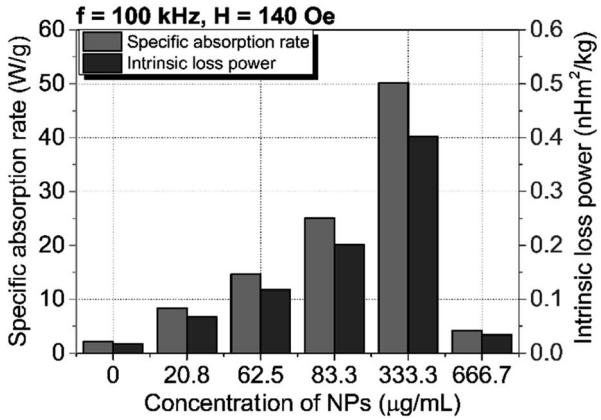


Fig. 7 Values of specific absorption rate and intrinsic loss power according to KBr concentration added to the synthesis of angle-shaped SPIONs.

in the temperature change. It can be said that the concentration of KBr affected the heating efficiency of the angle-shaped SPIONs. The angle-shaped SPIONs with optimized thermal properties can easily reach the thermal ablation zone ($\Delta T \geq 13$ °C)[43] for cancer treatment within 10 min. Angle-shaped SPIONs synthesized by adding 333.3 mM of KBr in the temperature change curve showed the highest temperature increase at 600 s. The SAR, defined as the mass and amount of energy converted to heat in unit time, quantifies the heating capacity of a magnetic material. The value of SAR can be calculated from the initial slope of the temperature rise graph using the following eqn (1)

$$\mathrm{SAR} = \frac{C_\mathrm{p}}{m_\mathrm{NP}} \times \frac{\Delta T}{\Delta t}\ \mathrm{W\ g^{-1}} \quad (1)$$

where $C_\mathrm{p}$ is the heat capacity of the solvent, $\Delta T/\Delta t$ is the initial heating rate, and $m_\mathrm{NP}$ is the mass of the magnetic component in the sample. Comparing this SAR value, the angle-shaped SPIONs synthesized by adding 333.3 mM of KBr (50.208 W $g^{-1}$) were 24 times higher than SPIONs synthesized without KBr (2.092 W $g^{-1}$). The value of the intrinsic loss power (ILP) was calculated at AMF of 100 kHz and 140 Oe based on the SAR calculated above using the following eqn (2)

$$\mathrm{ILP} = \frac{\mathrm{SAR}}{f \times H^2}\ \mathrm{nH\ m^2\ kg^{-1}} \quad (2)$$

where $f$ is the frequency and $H$ is the magnetic field. The ILP value of angle-shaped SPIONs synthesized by adding 333.3 mM of KBr (0.402 nH $m^2$ $kg^{-1}$) was about 24 times higher than SPIONs synthesized without KBr (0.017 nH $m^2$ $kg^{-1}$). The SAR and ILP of SPIONs synthesized using different concentrations of KBr were also calculated (Fig. 7 and S5, ESI†). The initial temperature rise over time is approximately linear and tends to decrease again after reaching the highest temperature. The initial rapid temperature rise can be attributed to the loss processes such as hysteresis loss, eddy current loss, Néel relaxation loss, and Brownian relaxation loss.[44] The mechanism of heat generation of magnetic nanoparticles by the alternating

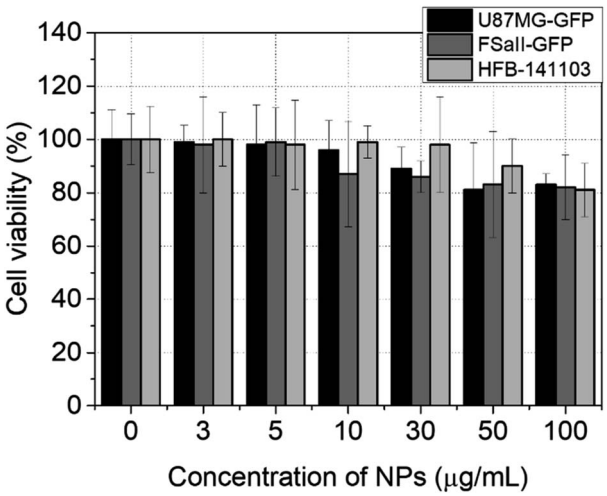


Fig. 8 Cell counting process results from three different types of cell lines (U87MG, FSall, and HFB-141103) for 24 h with an increase in the concentration of angle-shaped SPIONs (2 mmol KBr).

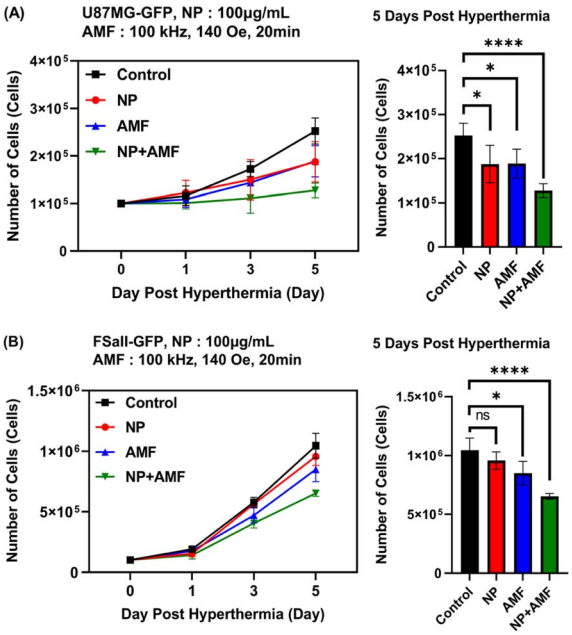


Fig. 9 Cell growth curves of cancer cell lines after *in vitro* magnetic hyperthermia test. (A) U87MG-GFP and (B) FSall-GFP cell lines were exposed to AMF, respectively (100 kHz, 140 Oe, and for 20 min).

magnetic field is different for magnetic nanoparticles having multi-domains and superparamagnetic nanoparticles having single domain configuration. Multi-domain magnetic nanoparticles are heated by hysteresis loss, and superparamagnetic nanoparticles are heated by Néel and Brownian relaxation loss.[45] Therefore, the cause of heat generation of angle-shaped SPIONs exhibiting superparamagnetic behavior is the Néel and Brownian relaxation loss. This indicates that superparamagnetic properties, such as the Néel rotation caused by the magnetic moment spin within the crystal structure of nanoparticles and the Brownian rotation occurring in the particle spin to align with the magnetic moment, are responsible for the majority of the measured total calorific value.

### 3.5. *In vitro* toxicity of angle-shaped SPIONs

The biocompatibility studies of the angle-shaped SPIONs were performed by cell counting using various concentrations of angle-shaped SPIONs. Three cancer cell lines, namely, U87MG, a type of glioblastoma, FSall, a primary cell line of fibrosarcoma, and HFB-141103, a primary cell of human fibroblast, were used to study the *in vitro* toxicity of the angle-shaped SPIONs. Because glioblastoma is located deep in the human body, there are limitations to the method using photothermal therapy (PTT). The light source for PTT is difficult to reach the location of the glioblastoma. However, MHT using a magnetic field can overcome this limitation.[46] Fibrosarcoma cells are tumor cells that are often used to verify the effectiveness of tumor treatment methods such as radiation therapy.[47,48] The data obtained after 24 h of cell culture are summarized in Fig. 8. The three cell lines showed some differences in their dependence of cell viability on the concentration of angle-shaped SPIONs, but cell viability remained high, exceeding 70% at all concentrations below 100 μg $mL^{-1}$. According to the International Organization for Standardization, Part 5: *in vitro* cytotoxicity test for medical devices (ISO 10993-5:2009 guideline), angle-shaped SPIONs at concentrations below 100 μg $mL^{-1}$ were considered to be non-cytotoxic to treated HFB-141103, U87MG, and FSall cell lines for 24 hours.

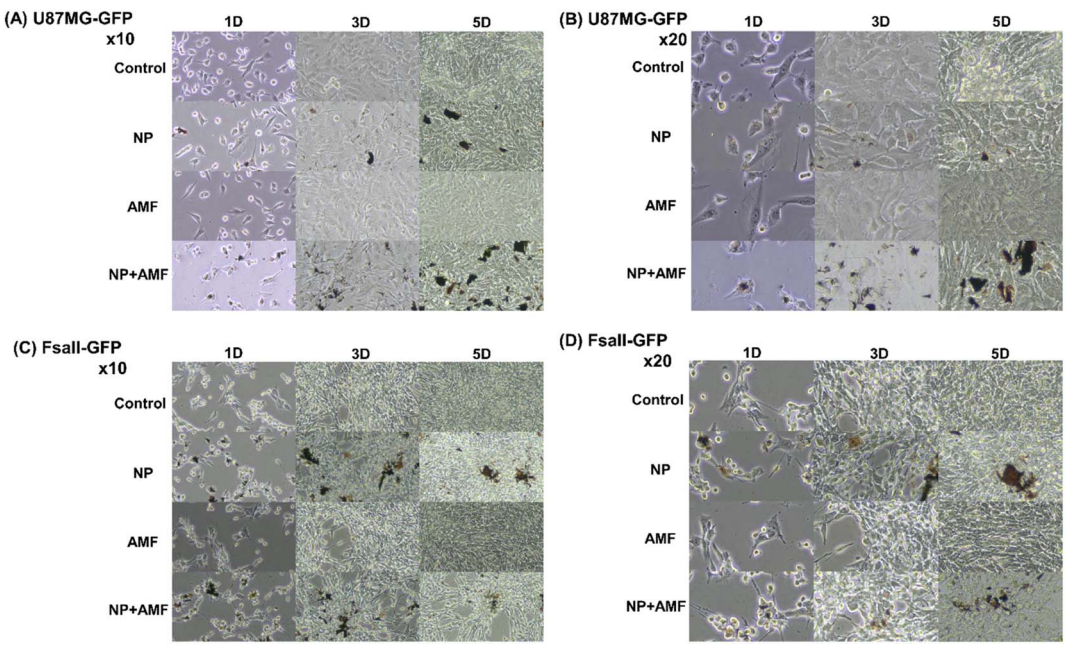


Fig. 10 Cell images of cancer cell lines after magnetic hyperthermia. (A) and (B) are images of U87MG-GFP cell lines, and (C) and (D) are FSall-GFP cell lines. AMF and NP + AMF groups are applied 100 kHz, 140 Oe. NP and NP + AMF groups were added angle-shaped SPIONs (100 μg $mL^{-1}$) to the medium.

### 3.6. *In vitro* hyperthermia test of angle-shaped SPIONs

Two cancer cell lines, U87MG and FSall, were used. Two cell lines were maintained on 37 °C and 5% $CO_2$ conditions of incubator for the prepared experiments. When cells were grown enough for experiments, $1 \times 10^6$ cells were moved to a 1.5 mL microtube and centrifuged to make a cell pellet. Then, the cells were redispersed in a culture media and media supplemented with angle-shaped SPIONs. Each medium was divided into the control group without any treatment, the NP group treated with angle-shaped SPIONs only, the AMF group applied AMF (100 kHz, 140 Oe) only, and the NP + AMF group treated with angle-shaped SPIONs and applied AMF (100 kHz, 140 Oe). The cell viability of the divided groups was measured on 1 day, 3 days, and 5 days.

Fig. 9 is a graph in which the number of cells in a tumor cell line was measured *in vitro* for 5 days. It can be seen that the cell growth rate of the other groups was slower than that of the control group. The cell growth rate of the NP group and the AMF group was statistically similar on U87MG but had a slight difference in FSaII. The NP + AMF group showed the lowest cell growth rate on both cancer cells. The metal uptake rate of cells is the difference according to the growth rate and the effect of AMF on each cell. In general, the growth rate of cancer cells is higher than that of normal cells; thus, metal uptake is higher for cancer cells than normal cells, and the penetrated into MHT efficiency is also better for cancer cells.[49–51] High-density MNPs through high intracellular metal uptake rate by AMF lead to MHT-induced apoptosis because they generated more thermal effects inside the cell membrane.[52,53]

Looking at the difference in the absorption rate of the nanoparticles between the NP group and the NP + AMF group in Fig. 10, it can be seen that the NP + AMF group had a higher absorption rate of nanoparticles than the NP group from the cell morphology of the microscopic image. This shows that the AMF exposure and heat generated by angle-shaped SPIONs improved the permeability of the extracellular matrix, allowing more nanoparticles to penetrate into the cells.[10] One MH treatment delayed the cell growth rate and decreased the cell viability. Intracellular NPs reduced the cell viability and growth rate.

## 4 Conclusion

In this paper, we reported the synthesis of angle-shaped SPIONs through the bromide-assisted polyol method, the difference in heat generation of SPIONs under external AMF, and the MH test using angle-shaped SPIONs. The saturation magnetization value of angle-shaped SPIONs synthesized by adding 333.3 mM KBr was evaluated to be 48.67 emu $g^{-1}$, which showed superparamagnetic behavior, indicating that it can be used for MH. Angle-shaped SPIONs showed different heating performances according to the concentration of bromide, and the SPIONs synthesized adding 333.3 mM KBr showed the highest temperature change ($\Delta T = 23.07$ °C). It also proved cytotoxicity in HFB-141103, U87MG, and FSall cell lines for up to 24 hours, and the results were fairly satisfactory. The measurement of cell viability of tumor cells U87MG and FSall showed the effect of MH therapy on angle-shaped SPIONs. When the angle-shaped SPIONs were injected and AMF was applied, it was shown to decrease the cell growth rate of the tumor cells compared to the control group. Based on these results, we expect that angle-shaped SPIONs will not only provide high-efficiency MH therapy application but also be used as a multifunctional platform for tumor treatment. Moreover, the method of synthesis can be applied to manufacture other useful nanomaterials for multiple biomedical applications.

## Author contributions

Hoonsub Kim and Pyung Won Im contributed equally to this work. Experiment design and perform: H. K., P. W. I., C. L., H. J. I., S. H. P., and Y. P. Writing and editing: H. K. and P. W. I. Data analysis: H. K., P. W. I., H. H., W. L., S. Y. P., and C. K. All authors read and approved the final manuscript.

## Conflicts of interest

There are no conflicts to declare.

## Acknowledgements

This research was supported by Basic Science Research Program through the National Research Foundation of Korea (NRF) funded by the Ministry of Education (NRF-2021R1A2C1008380), the Ministry of Science and ICT (NRF-2019M2D2A1A01058210, NRF-2020R1C1C1009000), and Nano Material Technology Development Program (NRF-2015M3A7B6027970). Also, this research was supported by the Korea Research Institute of Bioscience and Biotechnology (KRIBB) Research Initiative Program (KGM4562222) and Creative-Pioneering Researchers Program through Seoul National University (SNU). This work was partly supported by the Korea Institute of Energy Technology Evaluation and Planning (KETEP) grant funded by the Korea government (MOTIE) (20215710100170).

## Notes and references

1 M. Jeon, M. V. Halbert, Z. R. Stephen and M. Zhang, *Adv. Mater.*, 2021, **33**, 1906539.
2 D. Zhi, T. Yang, J. Yang, S. Fu and S. Zhang, *Acta Biomater.*, 2020, **102**, 13–34.
3 H. Y. Park, M. J. Schadt, L. Wang, I. I. S. Lim, P. N. Njoki, S. H. Kim, M. Y. Jang, J. Luo and C. J. Zhong, *Langmuir*, 2007, **23**, 9050–9056.
4 A. Moyano, E. Serrano-Pertierra, M. Salvador, J. C. Martínez-García, Y. Piñeiro, S. Yañez-Vilar, M. Gónzalez-Gómez, J. Rivas, M. Rivas and M. Carmen Blanco-López, *Biosensors*, 2020, **10**, 80.
5 J. R. Lee, B. W. Park, J. Kim, Y. W. Choo, H. Y. Kim, J. K. Yoon, H. Kim, J. W. Hwang, M. Kang, S. P. Kwon, S. Y. Song, I. O. Ko, J. A. Park, K. Ban, T. Hyeon, H. J. Park and B. S. Kim, *Sci. Adv.*, 2020, **6**, eaaz0952.
6 A. Espinosa, R. Di Corato, J. Kolosnjaj-Tabi, P. Flaud, T. Pellegrino and C. Wilhelm, *ACS Nano*, 2016, **10**, 2436–2446.

7 Z. Q. Zhang and S. C. Song, *Biomaterials*, 2016, **106**, 13–23.
8 A. E. Deatsch and B. A. Evans, *J. Magn. Magn. Mater.*, 2014, **354**, 163–172.
9 N. K. Prasad, K. Rathinasamy, D. Panda and D. Bahadur, *J. Mater. Chem.*, 2007, **17**, 5042–5051.
10 L. Beola, L. Asín, R. M. Fratila, V. Herrero, J. M. De La Fuente, V. Grazú and L. Gutiérrez, *ACS Appl. Mater. Interfaces*, 2018, **10**, 44301–44313.
11 V. I. Shubayev, T. R. Pisanic and S. Jin, *Adv. Drug Delivery Rev.*, 2009, **61**, 467–477.
12 C. S. S. R. Kumar and F. Mohammad, *Adv. Drug Delivery Rev.*, 2011, **63**, 789–808.
13 B. Mehdaoui, A. Meffre, J. Carrey, S. Lachaize, L. M. Lacroix, M. Gougeon, B. Chaudret and M. Respaud, *Adv. Funct. Mater.*, 2011, **21**, 4573–4581.
14 R. Hergt, S. Dutz, R. Müller and M. Zeisberger, *J. Phys.: Condens. Matter*, 2006, **18**, S2929.
15 C. Zhang, D. T. Johnson and C. S. Brazel, *IEEE Trans. Nanobioscience*, 2008, **7**, 267–275.
16 G. Azeh Engwa, P. Udoka Ferdinand, F. Nweke Nwalo and M. N. Unachukwu, Mechanism and Health Effects of Heavy Metal Toxicity in Humans, in *Poisoning in the Modern World – New Tricks for an Old Dog?*, ed. O. Karcioglu and B. Arslan, IntechOpen, London, 2019, pp. 77–100.
17 A. G. Roca, L. Gutiérrez, H. Gavilán, M. E. Fortes Brollo, S. Veintemillas-Verdaguer and M. del P. Morales, *Adv. Drug Delivery Rev.*, 2019, **138**, 68–104.
18 Q. Wang, X. Ma, H. Liao, Z. Liang, F. Li, J. Tian and D. Ling, *ACS Nano*, 2020, **14**, 2053–2062.
19 D. Toulemon, M. V. Rastei, D. Schmool, J. S. Garitaonandia, L. Lezama, X. Cattoën, S. Bégin-Colin and B. P. Pichon, *Adv. Funct. Mater.*, 2016, **26**, 2454–2462.
20 Z. Nemati, J. Alonso, I. Rodrigo, R. Das, E. Garaio, J. Á. García, I. Orue, M. H. Phan and H. Srikanth, *J. Phys. Chem. C*, 2018, **122**, 2367–2381.
21 S. Tong, C. A. Quinto, L. Zhang, P. Mohindra and G. Bao, *ACS Nano*, 2017, **11**, 6808–6816.
22 Y. Yang, X. Liu, Y. Lv, T. S. Herng, X. Xu, W. Xia, T. Zhang, J. Fang, W. Xiao and J. Ding, *Adv. Funct. Mater.*, 2015, **25**, 812–820.
23 A. K. Gupta and M. Gupta, *Biomaterials*, 2005, **26**, 3995–4021.
24 M. Cano, R. Núñez-Lozano, Y. Dumont, C. Larpent and G. D. La Cueva-Méndez, *RSC Adv.*, 2016, **6**, 70374–70382.
25 N. Zhu, H. Ji, P. Yu, J. Niu, M. U. Farooq, M. W. Akram, I. O. Udego, H. Li and X. Niu, *Nanomaterials*, 2018, **8**, 810.
26 A. A. Mieloch, M. Żurawek, M. Giersig, N. Rozwadowska and J. D. Rybka, *Sci. Rep.*, 2020, **10**, 2725.
27 K. M. Yang, H. Il Cho, H. J. Choi and Y. Piao, *J. Mater. Chem. B*, 2014, **2**, 3355–3364.
28 Z. Hedayatnasab, A. Dabbagh, F. Abnisa and W. M. A. Wan Daud, *Eur. Polym. J.*, 2020, **133**, 109789.
29 I. L. Hsiao, S. Fritsch-Decker, A. Leidner, M. Al-Rawi, V. Hug, S. Diabaté, S. L. Grage, M. Meffert, T. Stoeger, D. Gerthsen, A. S. Ulrich, C. M. Niemeyer and C. Weiss, *Small*, 2019, **15**, 1805400.
30 Y. Chu, R. Song, L. Zhang, H. Dai and W. Wu, *Int. J. Biol. Macromol.*, 2020, **153**, 46–54.
31 A. Khalid, A. Abdel-Karim, M. Ali Atieh, S. Javed and G. McKay, *Sep. Purif. Technol.*, 2018, **190**, 165–176.
32 A. Kolate, D. Baradia, S. Patil, I. Vhora, G. Kore and A. Misra, *J. Controlled Release*, 2014, **192**, 67–81.
33 O. Boussif, F. LezoualC'H, M. A. Zanta, M. D. Mergny, D. Scherman, B. Demeneix and J. P. Behr, *Proc. Natl. Acad. Sci. U. S. A.*, 1995, **92**, 7297–7301.
34 A. R. Vancha, S. Govindaraju, K. V. L. Parsa, M. Jasti, M. González-García and R. P. Ballestero, *BMC Biotechnol.*, 2004, **4**, 23.
35 S. M. Moghimi, P. Symonds, J. C. Murray, A. C. Hunter, G. Debska and A. Szewczyk, *Mol. Ther.*, 2005, **11**, 990–995.
36 H. Hatakeyama, H. Akita and H. Harashima, *Adv. Drug Delivery Rev.*, 2011, **63**, 152–160.
37 Z. Chen, Z. Lv, Y. Sun, Z. Chi and G. Qing, *J. Mater. Chem. B*, 2020, **8**, 2951–2973.
38 Z. Zhao, Z. Zhou, J. Bao, Z. Wang, J. Hu, X. Chi, K. Ni, R. Wang, X. Chen, Z. Chen and J. Gao, *Nat. Commun.*, 2013, **4**, 2266.
39 D. Yoo, C. Lee, B. Seo and Y. Piao, *RSC Adv.*, 2017, **7**, 12876–12885.
40 Z. Xu, C. Shen, Y. Tian, X. Shi and H. J. Gao, *Nanoscale*, 2010, **2**, 1027–1032.
41 S. Ghosh and L. Manna, *Chem. Rev.*, 2018, **118**, 7804–7864.
42 K. Woo, J. Hong, S. Choi, H. W. Lee, J. P. Ahn, C. S. Kim and S. W. Lee, *Chem. Mater.*, 2004, **16**, 2814–2818.
43 M. Nikfarjam, V. Muralidharan and C. Christophi, *J. Surg. Res.*, 2005, **127**, 208–223.
44 C. A. M. Iglesias, J. C. R. de Araújo, J. Xavier, R. L. Anders, J. M. de Araújo, R. B. da Silva, J. M. Soares, E. L. Brito, L. Streck, J. L. C. Fonseca, C. C. Plá Cid, M. Gamino, E. F. Silva, C. Chesman, M. A. Correa, S. N. de Medeiros and F. Bohn, *Sci. Rep.*, 2021, **11**, 11867.
45 Suriyanto, E. Y. K. Ng and S. D. Kumar, *Biomed. Eng. Online*, 2017, **16**, 36.
46 K. Mahmoudi, A. Bouras, D. Bozec, R. Ivkov and C. Hadjipanayis, *Int. J. Hyperthermia*, 2018, **34**, 1316–1328.
47 S. R. Khandelwal, P. S. Lin, C. E. Hall, Q. T. Truong, J. Lu, J. J. Laurent, G. S. Joshi, D. J. Abraham and R. K. Schmidt-Ullrich, *Radiat. Oncol. Invest.*, 1996, **4**, 51–59.
48 L. E. Gerweck, S. Vijayappa, A. Kurimasa, K. Ogawa and D. J. Chen, *Cancer Res.*, 2006, **66**, 8352–8355.
49 Q. Liu, J. Zhang, W. Xia and H. Gu, *Nanoscale*, 2012, **4**, 3415–3421.
50 A. J. Miao and W. X. Wang, *Mar. Ecol.: Prog. Ser.*, 2004, **275**, 103–113.
51 R. Wang, J. Liu, Y. Liu, R. Zhong, X. Yu, Q. Liu, L. Zhang, C. Lv, K. Mao and P. Tang, *R. Soc. Open Sci.*, 2019, **7**, 191139.
52 P. Das, M. Colombo and D. Prosperi, *Colloids Surf., B*, 2019, **174**, 42–55.
53 A. Jordan, R. Scholz, P. Wust, H. Fähling and R. Felix, *J. Magn. Magn. Mater.*, 1999, **201**, 413–419.